Brain Region-Specific Oligodendrocyte States Highlight Mitochondrial Gene Upregulation and Loss of Canonical Identity Signatures in Alzheimer's Disease

Francesca Drummer[1,2,3], Nadia Dorosti[3,4], Charlene Hurler[3], Eduardo Beltrán[5,6,7], Louis B. Kümmerle[1,8,9], Fabian Theis[1,2], Sarah Jäkel[3,6,10,*]

[1]Institute of Computational Biology, Helmholtz Center Munich, Germany.
[2]School of Computing, Information and Technology, Technical University of Munich, Munich, Germany
[3]Institute for Stroke and Dementia Research, LMU Hospital, LMU Munich, Germany
[4]Graduate School for Systemic Neurosciences, LMU Munich, Germany
[5]Institute of Clinical Neuroimmunology, University Hospital, Ludwig Maximilian University of Munich, Munich, Germany
[6]Munich Cluster for Systems Neurology (SyNergy), Munich, Germany
[7]Biomedical Center (BMC), Faculty of Medicine, Ludwig Maximilian University of Munich, Martinsried, Germany
[8]TUM School of Life Sciences Weihenstephan, Technical University of Munich, Germany.
[9]Institute for Intelligent Biotechnologies, Helmholtz Munich, 85764 Neuherberg, Germany
[10]Department of Psychiatry and Psychotherapie, TUM School of Medicine and Health, Munich, Germany

[*]Correspondence to sarah.jaekel@med.uni-muenchen.de

Abstract

Oligodendrocyte dysfunction and heterogeneity are emerging as key contributors to Alzheimer's disease (AD) pathology, though cellular mechanisms remain unclear. Using single-nucleus RNA sequencing across three cortical regions from the same individuals, we identified region- and disease-specific transcriptomic changes, including increased mitochondrial genes and loss of cell type signatures. These results highlight the importance of biologically-informed quality control and underscore the value of multi-regional analysis for understanding AD pathogenesis and progression.

Main text

Emerging evidence has identified oligodendrocytes (OL) as a noteworthy cell type in the etiology of Alzheimer's disease (AD)[1]. Although, thus far, transcriptomic studies have pointed to oligodendroglial dysfunction in AD, the pathomechanisms leading to their dysfunction and driving the progression of the disease across different cortical regions remain largely elusive.

To investigate brain region-specific transcriptomic changes of OL in AD, we performed single nucleus RNA-Sequencing (snRNA-seq) on post-mortem human brain tissue of six AD patients and age- and sex-matched controls each with an APOE ε3/ε3 background. Cortical grey matter samples partially depleted of neurons were collected from three areas per donor: prefrontal, temporal, and visual cortices (PFC, TC and VC, respectively). These regions were chosen to represent a snapshot of the temporal progression of the disease with the VC serving as a minimally affected internal control[2] (Fig. 1A, Extended Data Table 1). Unlike previous studies, the present approach analyzes differently affected regions from the same donor, enabling cellular comparisons across disease progression, which has so far not been performed, especially in regard to OL.

After quality control (Extended Data Fig. 1, Extended Data Table 2), the remaining 26.598 nuclei clustered into seven major cell types by the expression of established canonical marker genes: OL (9.030 nuclei, *OLIG2*, *SOX10*), oligodendrocyte precursor cells (OPC, 2.530 nuclei, *PDGFRA*, *VCAN*), microglia (2.262 nuclei, *APBB1IP*, *C3*), astrocytes (6.420 nuclei, *SLC1A2*, *GFAP*), subtypes of both excitatory (2.377 nuclei, *CUX2*, *SLC1A7*) and inhibitory neurons (2.221 nuclei, *GAD1*, *GAD2*), endothelial cells (EC, 1240 nuclei, *CLDN5*, *FLT1*) and vascular leptomeningeal cells (VLMC, 518 nuclei, *COL1A1*, *COL1A2*) (Fig. 1B-F). Similarly to another study[3] we observed mixed lineage clusters (Extended Data Fig. 2A-D, Extended Data Table 3). Although these might confer biological function, as demonstrated by co-expression of CD31 and CNP in some cells in the human brain (Extended Data Fig. 2E) we removed them in our analysis to focus on established OL clusters. Whilst disease condition did not influence proportional cluster abundance, assignment to a specific brain region did (Fig. 1E), likely due to different cellular architectures and functional specializations[4,5].

In accordance with other studies[6–8], we did not observe significant changes in cell type proportions in AD compared to control donors within the same region (Fig. 1E). When shifting our focus to OLs, contrary to what is commonly demonstrated by histological analysis[9,10], we did not capture a loss of these cells in the disease condition, which was surprising as tissue-based microscopy approaches are better in determining cell frequencies. In fact, whilst most cell types remained stable across brain regions, we found a slight increase in OL proportions in the PFC and TC. To validate OL numbers and to identify whether there are further discrepancies between bioinformatic and histological analyses, we chose to immunohistochemically assess OL lineage cells (OLIG2) and mature OL (CNP) and EC (CD31) (Fig. 1G,H, Extended Data Fig. 3A,B) in a different patient cohort. Whilst OLIG2 and CNP+ OL were overall not changed between conditions, lower layers of the TC exhibited significantly higher numbers of mature OL, which supports our bioinformatic analysis and a recent live-imaging study that reported different OL densities in different cortical areas in rodents[11]. CD31+ EC however, showed a clear trend towards being increased in AD, which were not captured by our bioinformatic analysis. In brief, these data emphasize the importance of performing immunohistochemical validations to corroborate bioinformatic findings, and highlight compositional differences between different cortical regions.

Although OLIG2 numbers were not significantly changed in our analysis in AD, we observed weaker OLIG2 signals within cells during our analysis, raising the hypothesis that canonical marker expression and therefore the characteristic cell type signature might be lost in disease. Indeed, further validations using OLIG2/SOX10 and CNP confirmed a significant increase in the number of SOX10- or OLIG2- CNPase+ OL (Fig. 1G). We then

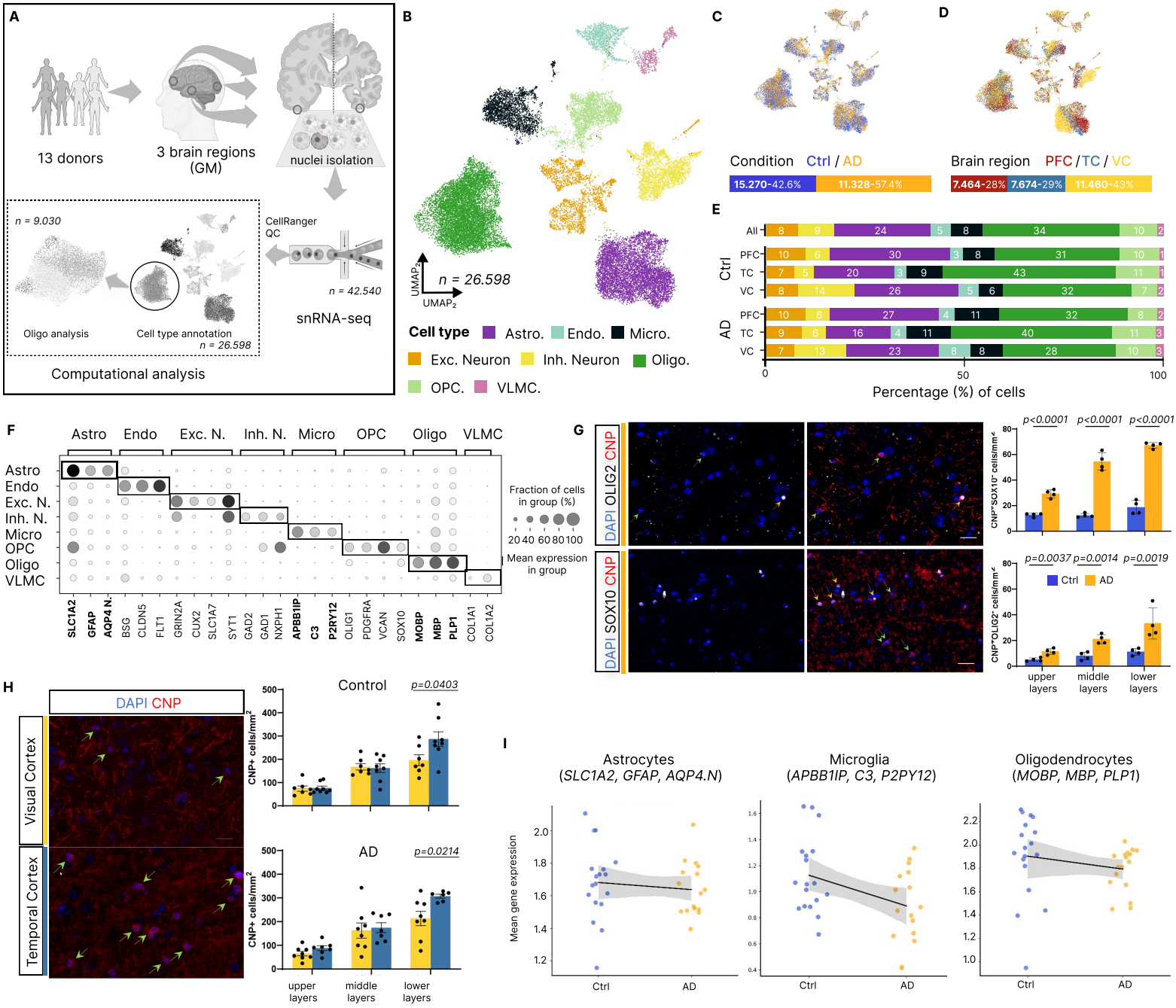

Figure 1: Cell type specific transcriptional profiles diverge across brain areas in AD pathology.

A Study design showing snRNA-seq analysis of 13 donors across 3 brain regions (prefrontal, temporal and visual cortex) with nuclei isolation and sequential computational analysis of oligodendrocytes. **B-D** UMAP visualizations of all cell types after QC (n = 26,598 nuclei), with major cell populations (**B**), conditions - AD vs Control - (**C**) and cortical areas **(D**). E Percentage distribution of cellular composition across conditions and cortical areas (PFC, TC, VC). **F** Dotplot of selected marker genes for broad cell type annotation. **G** Representative immunofluorescence images of AD patient brains and quantifications of CNP+ OLIG2-/SOX10- oligodendrocytes in human brain tissue (n = 4 individuals per group), demonstrating a decrease of canonical marker expression in oligodendrocytes in AD. Scale bar = 50µm. **H** Quantifications of CNP+ oligodendrocytes (green arrows) across cortical layers in the visual and temporal cortices in control and AD brains (n = 7-8 individuals per group). Scale bar= 20µm. **I** Mean expression of canonical marker genes for astrocytes, microglia and oligodendrocytes between control and AD, demonstrating a general loss in AD.

quantified the expression of canonical marker genes for each cell type used for cluster annotation (Fig. 1F) and found a lower mean expression for OL, as well as for some other cell types across and within brain areas in AD (Fig. 1I, Extended Data Fig. 3C, Extended Data Table 4). Canonical marker genes were especially reduced in OLs in the TC and VC, which was quite unexpected, as the VC is generally expected not to be heavily impacted by the pathology[2]. Therefore, our bioinformatic data support the hypothesis of changed cell type signatures with decreased canonical marker gene expression. This finding might explain the discordance in the number of OL in AD between histopathological and transcriptional studies, as cluster annotation in snRNA-seq data does not solely rely on a single canonical cell marker.

Interestingly, we observed an increase in mitochondrial (MT) gene fraction over all cells with increasing Braak stages (Fig. 2A). Uniform MT gene fraction filtering is classically used as a quality control (QC) criterion[12], however a recent study[13] demonstrated a significant higher baseline MT gene fraction in cancer vs healthy cells. Therefore adaptive[14] or nuclear fraction thresholding, such as MALAT1[15] has been suggested as an alternative QC assessment. After confirming less variation of MALAT1 as compared to MT-fraction, across Braak stage in our data (Fig. 2A,B, Extended Data Fig. 4A), we applied biologically informed thresholding (Suppl. Tab 2), driven by condition and region (Extended Data Table 5), showing that MALAT1, MT-thresholding and other QC criteria consider different cells as low quality (Extended Fig. 4B). Subsequently, we still observed a high overall *MALAT1* expression across cells, but cell type specific proportions of low (<0.15) and high MT-fractions (>0.15) (Fig. 2C), with excitatory neurons and OL being on the higher end, and astrocytes and endothelial cells on the lower end. Further analysing MT-fraction across cortical areas in our data (Fig 2B) and Gabitto et. al, 2024[16] (Extended Data Fig. 4D), we found an increase from PC to TC to VC , which we also observed in our Visium spatial transcriptomics data (Fig. 2D, Extended Data Fig. 5). If elevated MT-fraction represented poor sample quality, brain regions within the same donor would show a similar MT-fraction level. As the VC is affected later and less heavily by AD pathological burden than the PFC and TC, we would expect higher MT-fractions in PFC and TC due to a higher abundance of stressed and dying cells. Hence, our data demonstrate a condition-specific upregulation of MT-genes. Moreover, the MT-gene fraction along all Braak stages in another dataset (Extended Data Fig 4C) also suggests an upregulation in the earlier stages of the disease (Braak stage 3). Cellular stress has been reported to tether mitochondria to the nucleus to aid survival[17], which might be a biological explanation of why in some cells and areas more MT-genes can be detected in sn-RNA-seq data in disease.

Within all OL nuclei, we identified four unique OL states (Fig. 3A), of which none was exclusively associated with any singular sample variable, such as condition or cortical area (Fig. 3B), but we observed higher similarity between OL in TC and VC in comparison to PFC (Fig. 3C). This observation demonstrates global area-specific heterogeneity which might be related to OL function, in the case of promoting extracellular plasticity or circuit remodelling[18,19]. Interestingly, the PFC did not stand out in terms of composition of all cell types: for example GABAergic neuron composition mostly differed in the VC (Extended Data Fig 6). This finding highlights important structural differences between different cortical areas and exemplifies why analysing a single cortical brain region by snRNA-seq, as commonly practiced, and then extrapolating the results to other brain regions should be done cautiously.

For each OL state, we identified up- and down-regulated genes (Fig. 3D) finding unique gene signatures per cluster (Fig. 3E): Oligo1 (4.557 nuclei, *LAMA2*, *LRP6*), Oligo2 (3.711 nuclei, *MT-ND4*, *MT-ND3*), Oligo3 (460 nuclei, *FRY*, *MDGA2*) and Oligo4 (199 nuclei, *PIEZO2*, *DHCR24*, *RBFOX1*). When compared to Gabitto et al., 2024[16] that have the same OL subtype resolution, we observed a large agreement for cluster-specific upregulated genes (Fig. 3F). Gene Set Enrichment Analysis (GSEA)[20] (Fig. 3G) of these clusters revealed functional differences, with Oligo1 being characterized by cell-cell interactions, Oligo3 by synaptic signalling and Oligo4 by morphological changes, cholesterol metabolism and intracellular transport. The latter RBFOX1-

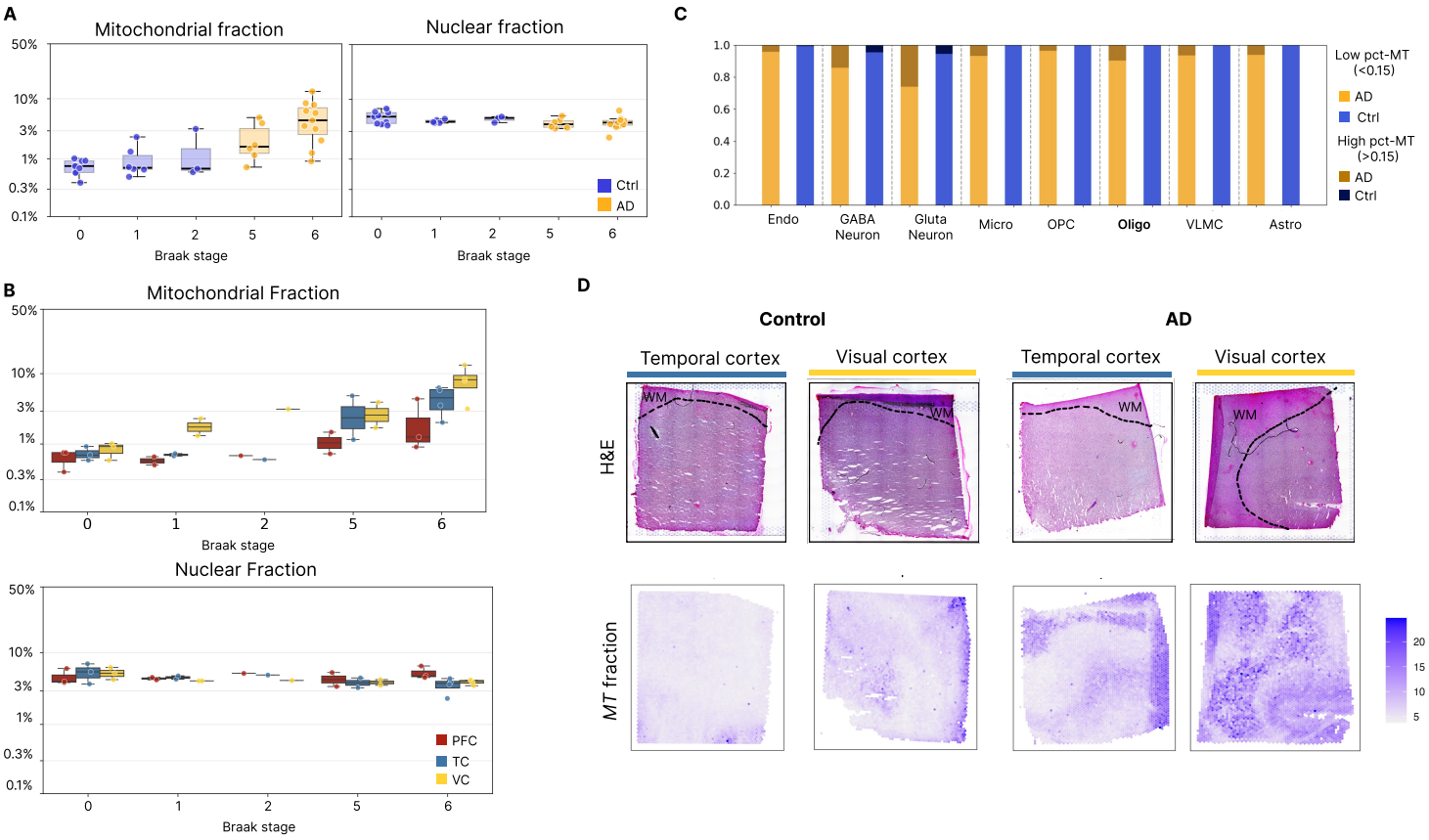

Figure 2: Mitochondrial gene expression varies across cortical areas and in disease.

Pre-quality control analysis showing percentage of mitochondrial (MT) and nuclear fractions for all cells across different Braak stages (**A**) and different cortical regions (**B**). **C** The percentage of low (<15%) and high (>15%) MT fraction shown per cell type and condition. **D** Visium analysis of temporal and visual cortices from control and AD brain samples. Upper panels show H&E staining with cortical layers and gray matter (GM) boundaries marked. Lower panels display spatial distribution of MT gene fractions across tissue sections.

expressing Oligo4 cluster specifically mapped to the (immature) Oligo_1 from Gabitto et al. 2025 and was also reported in previous studies[21–23]. The genes related to high cholesterol metabolism point towards actively myelinating cells, the high abundance of *RBFOX1*, which is also highly expressed in neurons[24] and in OL-neuron mixed lineage cells (Extended Data Fig. 2B), further pointing towards a neuromodulating function of Oligo4. Oligo2, on the other hand, which also showed an enrichment in AD (Fig. 3B), was predominantly characterized by the absence of cellular interactions, with a simultaneous upregulation of *MT* genes, as highlighted in previous research[21,22]. The aforementioned *MT*-gene upregulation is associated with disease and might result in the loss of important cellular functions, for instance, a loss of OL-axonal coupling or myelin maintenance. MT-ND4 in particular has recently been suggested as a promising biomarker of AD[25]. IHC validations in a different patient cohort corroborated a higher abundance of MT-ND4+ OL in the TC of AD subjects as compared to controls (Fig. 3H). In contrast, other prominent disease-associated OL markers from the literature[26–29], such as *SERPINA3*, could not be observed (Extended Data Fig. 7). While this could be due to technical reasons (e.g. sequencing depth or single nucleus vs single cell analysis)[30], we hypothesize that these markers are species-specific, as *SERPINA3* has predominately been reported in mouse models and not consistently in humans[7,22].

In conclusion, our work reveals functional differences between OL states, which in AD show a loss of essential functions such as myelin maintenance, axonal support, and metabolic processes. We identify mitochondrial activation as a general hallmark of disease progression, demonstrating that up-regulation of mitochondrial genes is not merely a technical artifact but reflects underlying pathology. Additionally, we show that the loss of characteristic cell signatures in AD suggests widespread changes in cellular functions across multiple cell types. Together, these findings advance our understanding of the cellular mechanisms driving AD pathogenesis and lay the groundwork for developing targeted therapies to restore oligodendrocyte health and function.

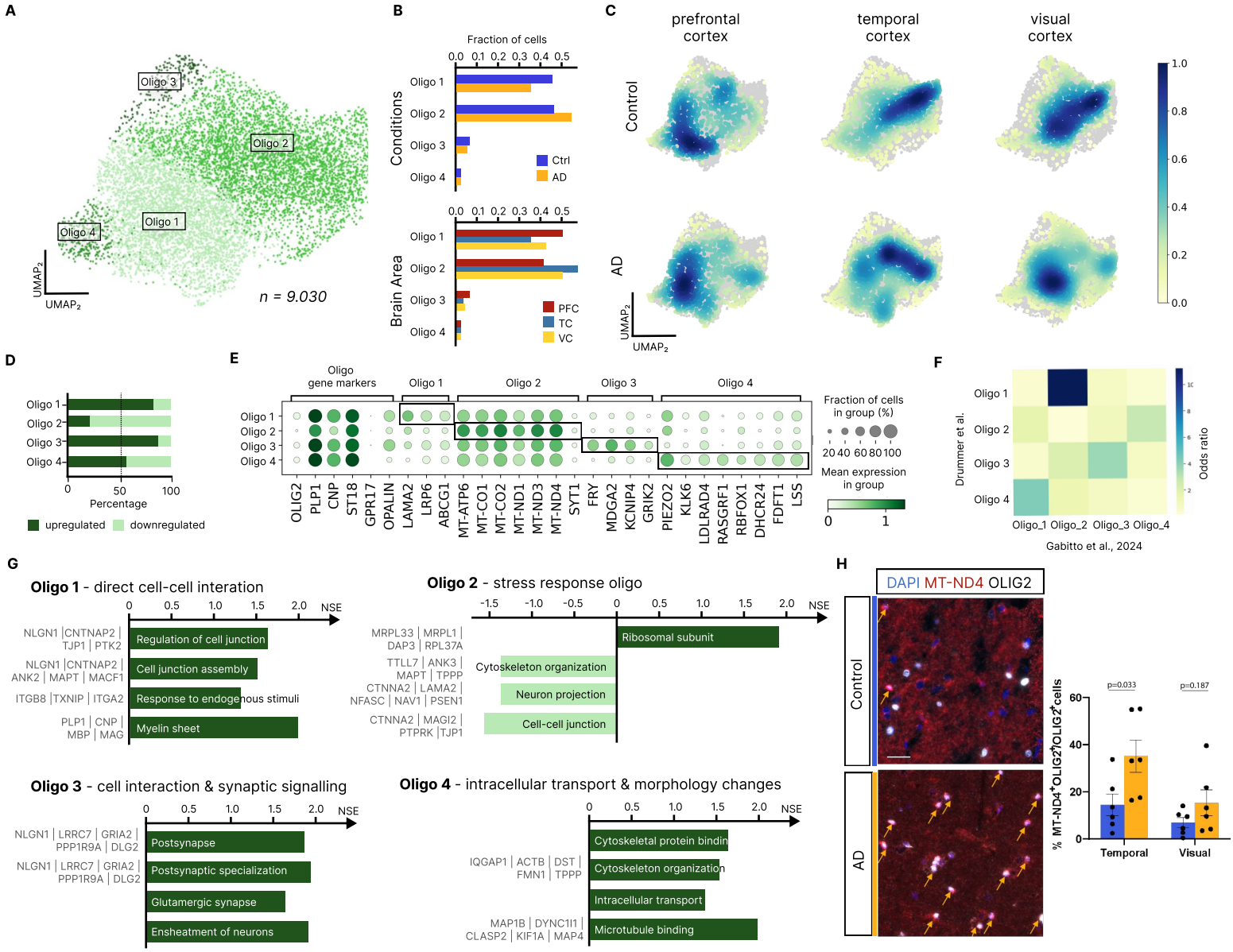

Figure 3: Oligodendrocyte subtypes vary across cortical areas and in disease.

A UMAP plot of oligodendrocyte suptypes (n= 9030). **B** Bar plots depicting the fraction of cells per condition and area distributed across OL subtypes. **C** UMAP plots of OL with gaussian kernel density estimates over area and condition. **D** Bar plot depicting the percentage of up- and down-regulated differentially expressed genes (adjusted p-value < 0.05) across oligodendrocyte subtypes identified with DESeq2. **E** Dotplot showing oligodendrocyte subset markers based on DE analysis. **F** Heatmap showing the confusion matrix comparing OL annotations with a recently published reference dataset16. **G** Functional characterization of OL subclusters via pathway analysis, indicating normalized expression scores (p-value < 0.05) from each pathway; selected relevant genes of each pathway are displayed on the left. **H** Representative images and quantifications of MT-ND4+ OLIG2+ oligodendrocytes in the temporal and visual cortices of post-mortem human brains (n = 6 individuals per group). Scale bar = 25µm.

137 **Methods**

138 **Human subjects**

139 Post-mortem tissue for this project was obtained from The Edinburgh brain bank, the Newcastle brain bank
140 and the Munich brain bank with ethical approval from the Ethics Committee at the LMU Munich (vote 22-
141 1060).

Donor ID	Condition	Sex	Age	Tissue Source
Frozen Tissue samples for snRNAseq and Visium analysis				
Ctrl3	Control	male	70	Neurobiobank Munich
Ctrl4	Control	male	76	Neurobiobank Munich
20130894	Control	male	80	Newcastle Brain Resource
20110891	Control	male	73	Newcastle Brain Resource
20100742	Control	male	67	Newcastle Brain Resource
SD030/18	Control	male	63	Edinburgh Brain Bank
SD006/14	Control	male	60	Edinburgh Brain Bank
20185928	Alzheimer's Disease	male	69	Newcastle Brain Resource
20174945	Alzheimer's Disease	male	69	Newcastle Brain Resource
AD3	Alzheimer's Disease	male	70	Neurobiobank Munich
AD5	Alzheimer's Disease	male	74	Neurobiobank Munich
AD6	Alzheimer's Disease	male	77	Neurobiobank Munich
AD7	Alzheimer's Disease	male	75	Neurobiobank Munich

142

143 **snRNA-seq pipeline**

144 **Nuclei sampling and library preparation**

145 Fresh-Frozen tissue blocks were cut into 20µm sections and Luxol-Fast-Blue stainings were performed to
146 determine tissue architecture. Gray Matter regions from ~10-20 sections per sample were collected using a
147 razor blade. Nuclei isolation was performed with a nuclei isolation kit (Nuclei EZ Prep; NUC101; Sigma
148 Aldrich) according to the manufacturers instructions and nuclei underwent FACS sorting for NeuN
149 (FCMAB317PE; Merck) and DAPI. To enrich our samples for GM cells, we collected 10.000 DAPI+NeuN+ nuclei
150 and 10.000 DAPI+NeuN- negative nuclei per sample to precede with the library preparation.

151 **Library preparation and Sequencing**

152 Samples were randomly distributed to 10X Genomics Chromium single cell 3' chips. LIbraries were prepared
153 with the 10X Genomics v3 beads, Gem kits and library kits, according to the manufacturer's instructions.
154 Library quality and final concentrations were determined using a Bioanalyzer.

155 For sequencing, libraries were again randomized and 9-10 libraries were combined at equimolar
156 concentrations and adjusted to 2nM for sequencing on a NovaSeq S4 Flowcell with a targeted sequencing
157 depth of 50K reads per nucleus at the Competence Centre for Genomic Analysis in Kiel. To avoid sequencing
158 batch effects, each pool was sequenced twice on different lanes and the results were combined.

159 **snRNA-seq preprocessing, QC and annotation**

160 We followed the best practices single-cell analysis suggestions from Heumos et al., 2023[12] and their updated
161 online resource: https://www.sc-best-practices.org/preamble.html.

162 **snRNA-seq data preprocessing**

163 Gene counts were obtained by aligning reads to the GRCh38 (hg38) Genome Ensembl 105 using Cell Ranger
164 software (v.9.0.0) (10x Genomics). The filtered cell ranger matrix contains 42.540 cells and 78.932 genes
165 (Supp. Table 1). First, we filter low quality cells given cell clusters that are associated with low number of
166 detected genes, low count depth or high fraction of mitochondrial counts using Scanpy[31]. Additionally, we
167 consider *MALAT1* expression of the cells which is related to the nuclear fraction of cells captured[32]. During
168 this preprocessing step we mainly remove cells from the three samples AD3 - GR, AD5 - AS and Ctrl6 - GR that
169 are associated with low number of cell counts and genes according to cellranger (Supp. Table 1) and
170 distribution plots (Suppl. Fig 1).

171 From initial observations there are expression and count differences between condition and brain area
172 samples that we suspect to be biological rather than technical (difference in mean but rather stable standard
173 deviation). Therefore, we apply sub-group specific thresholds per condition and brain area for a biology
174 inspired data-driven quality control[14] (Suppl. Tab 2). To account for ambient RNA we corrected gene counts
175 using SoupX[33], removing 44.117 genes and we removed 898 cells from high count doublet clusters (>0.9)
176 detected by scublet[34]. Another cluster with higher than average doublet count was kept, because it contains
177 OPCs that have a higher transitional profile which are possibly mistaken as doublets and the lower amount
178 of doublets expected in single-nuclei data.

179 **Normalization and dimensionality reduction**

180 Functions in the Scanpy[31] (v1.10.4) package were used for the following analyses. First we selected highly
181 variable genes (2k) and then normalised the counts to the median of total counts for observations (cells)
182 before normalization. As suggested by a recent benchmark[35], we applied a shifted logarithm transformation
183 $log\ (\frac{y}{s} + y_0)$ on the raw counts y with a size factor s and pseudo-count y_0. After scaling the data, we
184 performed Principal Component Analysis (PCA) with 50 PCs followed by Uniform manifold approximation and
185 projection (UMAP) based on their 15 neighborhood embeddings.

186 **Batch analysis and integration**

187 For integration, we first determined which covariates cause batch effects in the dataset. We included
188 technical (e.i. brain bank source, donor) and biological covariates (e.i. Braak stage, cortex area) in the analysis.
189 To quantify the contribution of covariates we performed Principal Component Regression (PCR) using
190 scAtlasTB[36] (https://github.com/HCA-integration/scAtlasTb/). We considered four covariates and computed
191 the variance explained (PRC) by each covariate across the top principal components of the gene expression
192 matrix, comparing observed values against a null distribution generated by permutation (N=30). Significant
193 covariates were identified based on z-scores and empirical p-values. The donor identity accounted for the
194 largest variance (pcr = 0.045, z = 4.48, n = 12, p < 0.01), followed by brainbank source (pcr = 0.013, z = 3.50,

195 n = 3, p < 0.01), Braak stage (pcr = 0.010, z = 3.09, n = 5, p < 0.01), cortex area (pcr = 0.010, z = 2.52, n = 3, p
196 < 0.05), and condition (pcr = 0.009, z = 2.87, n = 2, p < 0.05).

197 To remove the technical batch effects we integrated on donor and brain bank sources using scVI[37], scANVI[38].
198 We evaluate the data integration with metrics from scIB[39,40] to compare biological and technical batch
199 removal. Finally, the scVI integrated data on donors was chosen as the most meaningful representation.

200 **Clustering and cell type annotation**

201 Clustree[41] (v.0.4.1) was used to select the most stable clustering resolution (res=1.0) for the overall. Using
202 sc.tl.leiden with resolution 1.0 we obtained 28 clusters on the full dataset. Cluster 26 and 27 were removed
203 due to low cell counts (8 and 39 cells respectively) (see Supp. Table 2). To identify major cell types, we
204 assigned clusters to cell types according to cell-type specific markers from literature [6,7,21,42]. Next we saved
205 the raw count data in .h5ad format and the deep generative mapping algorithm from MapMyCells (RRID:
206 SCR_024672) was used to align the nuclei with the 10x human MTG reference (CCN20230505). The mapping
207 results were projected onto the leiden clustering and a cluster was assigned to a cell type if the mapped
208 fraction of one cell type was higher than 0.75 (Suppl. Table 4). Most mapped annotations agree with the
209 manual annotations. A subset of 2.670 cells were not able to be associated with a specific cell type cluster,
210 indicating mixed-lineage clusters (Suppl. Figure 3). According to the cell type mapping, this subset mainly
211 seems to consist of Glutamatergic Neurons, Oligodendrocytes, Microglia and Astrocytes.

212 The final data cohort consists of a total of 26.598 nuclei across 6 controls (15.270 cells) and 6 AD patients
213 (11.328 cells) with 34.802 genes, with a median of 10.354 counts and 3.086 features per nucleus.

214 **Differential gene expression analysis**

215 Differential gene expression analysis was performed using the DESeq2[43] package (v.1.48.1) in R (v.4.5.1).
216 Gene expression count matrices and associated metadata were prepared from single-cell RNA sequencing
217 data. To avoid issues with zero counts, a pseudocount of 1 was added to all expression values and low
218 expression genes were filtered if they had at less than 10 counts in a minimum of 3 samples. We performed
219 i) one-vs-all and ii) pairwise comparisons. For the one-vs-all comparison, each experimental condition was
220 compared against all other conditions combined while the pairwise comparison compared conditions (AD,
221 Ctrl) in the same biological context (e.i. cortical areas).

222 Results were summarized to report the total number of genes tested, significantly upregulated genes
223 (positive log2 fold change, FDR < 0.05), and significantly downregulated genes (negative log2 fold change,
224 FDR < 0.05) for each comparison. Furthermore, we visualize the results with volcano plots showing the
225 change in expression on the x-axis (log-fold-change) and statistical significance on the y-axis (FDR-corrected
226 p-values). We color code the genes that have a FDR-corrected p-value under 0.01 and log-fold-change over
227 1.5.

228 **Gene Set Enrichment Analysis**

229 Functional annotation of gene sets was performed with Fast Gene Set Enrichment Analysis (fgsea)[20] on each
230 oligodendrocyte cluster using the differentially expressed gene lists. The gene pathways from Molecular
231 Signatures Database (MSigDB)[44] were used specifically H, C2 and C5, which is the gene ontology collection.
232 For each oligodendrocyte cluster we pre-filtered pathways with a p-value < 0.05 and then selected 4
233 representative pathways for each cluster with associated genes.

234 **Compositional Analysis of cell types**

235 We ran scCoda[45] for the compositional analysis using the pertpy framework (v1.0.0)[46] to compare the relative
236 abundance of major cell types. We ran the analysis across four different covariate combinations: 1) condition
237 across all brain areas and 2) within brain areas, 2) brain region and 3) combined condition and brain area.
238 The recommended false discovery rate (FDR) value from pertpy for the scCoda analysis is 0.2. To receive
239 credible effects for condition (AD vs Ctrl) analysis (1,2) we needed to increase the FDR to 0.5. For the other
240 covariates that involve cortex area differences a FDR of 0.2 was sufficient. Because there is no consensus on
241 which supertypes would be affected by AD, we ran the compositional analysis with each cell type set as the
242 unchanged reference population, as recommended by the authors of scCODA. The final results were
243 averaged across reference cell types (Supp. Table 3).

244 **Canonical marker gene expression differences**

245 For canonical marker genes to accurately identify cell types their expression must be high in the cell type
246 clusters. As cell type annotation mapping was performed before integration some clusters contain an
247 unbalanced amount of Ctrl vs AD cells. We observed a general trend that clusters with a higher Ctrl fraction
248 could be more accurately mapped. One potential reason could be a decrease of canonical marker gene
249 expression with an increase of disease related genes that are also considered canonical marker genes (e.i.
250 CLU - astrocyte marker but also a myelination gene that is known to decrease during AD progression). We
251 compare canonical gene marker expression sample wise between conditions (Fig. 1G).

252 **Mitochondrial and nuclear gene fraction processing**

253 Gene expression fractions were calculated at the sample level by aggregating specific gene sets and total
254 gene counts across all cells within each sample. To improve visualization of differences in low fraction ranges
255 where most samples typically fall and numerical stability, we applied a logit transformation following the
256 formula: logit_fraction = logit((target_genes + 1)/(total_genes + 2)), where target_genes represents the sum
257 of counts for the gene set of interest and total_genes represents the sum of total gene counts per sample,
258 and added pseudocounts.

259 Data were visualized using grouped boxplots with individual sample points overlaid, stratified by
260 experimental conditions. The logit-transformed y-axis was displayed with percentage labels (0.1%, 0.3%, 1%,
261 3%, 10%, 50%) to facilitate interpretation while maintaining the improved resolution in the low percentage
262 range.

263 For mitochondrial fraction analysis, mitochondrial genes comprised 37 mitochondrial-encoded genes (*MT-*
264 *TF, MT-RNR1, MT-TV, MT-RNR2, MT-TL1, MT-ND1, MT-TI, MT-TQ, MT-TM, MT-ND2, MT-TW, MT-TA, MT-TN,*
265 *MT-TC, MT-TY, MT-CO1, MT-TS1, MT-TD, MT-CO2, MT-TK, MT-ATP8, MT-ATP6, MT-CO3, MT-TG, MT-ND3,*
266 *MT-TR, MT-ND4L, MT-ND4, MT-TH, MT-TS2, MT-TL2, MT-ND5, MT-ND6, MT-TE, MT-CYB, MT-TT, MT-TP*). For
267 nuclear fraction analysis, nuclear markers included 30 nuclear-encoded genes (*MALAT1, NEAT1, FTX, FOXP1,*
268 *RBMS3, ZBTB20, LRMDA, PBX1, ITPR2, AUTS2, TTC28, BNC2, EXOC4, RORA, PRKG1, ARID1B, PARD3B, GPHN,*
269 *N4BP2L2, PKHD1L1, EXOC6B, FBXL7, MED13L, TBC1D5, IMMP2L, SYNE1, RERE, MBD5, EXT1, WWOX*).

270 **Oligodendrocyte subclusters comparison with Gabitto et al., 2024**

271 To compare the oligodendrocyte subclusters with the oligodendrocyte subclusters from Gabitto et al., 2024[16]
272 we used the up- and downregulated DE genes identified per cluster. The DE genes in Gabitto et al., 2024 were
273 calculated with Nebula[47] while we used DESeq2.

To systematically assess the overlap between DE gene signatures, we performed enrichment analysis using Fisher's exact test. First, we separated genes into upregulated and downregulated sets based on their log fold change values. We defined the analysis universe as the intersection of all genes detected in both datasets to ensure appropriate statistical comparison. For each direction combination (up-up, up-down, down-up, down-down), we calculated the overlap between gene sets and performed one-sided Fisher's exact tests and calculate the odds ratios to quantify the strength of association between gene sets and applied false discovery rate (FDR) correction using the Benjamini-Hochberg procedure to account for multiple testing across the four directional comparisons.

Visium analysis

Visium pipeline and sequencing

For the visium pipeline, 4 of the best samples from the snRNA-seq experiment were chosen and small blocks were further processed for the 10x Genomics Visium Spatial Gene Expression pipeline and the protocol was performed according to the manufacturer's instructions. Libraries were assessed by a bioanalyzer and sequenced with a NextSeq 2000 P3 Flowcell with a sequencing depth of 400K reads per sample.

Quality control

For spatial validation of the condition and brain area specific effects we obtained data from one Visium slide with 4 images from one control and one AD patient for each temporal and visual cortex respectively. Gene counts were obtained by aligning reads to the GRCh38 (hg38) Genome Ensembl 105 using Space Ranger software (v.2.1.1) (10x Genomics). We performed basic quality control (removed zero count genes) followed by a locally aware quality control using SpotSweeper[48] to account for region specific trends per sample independently. For further statistical testing more replicates are needed, hence we are only using it as support for our other findings.

The MT fraction was calculated using a subset of 13 MT-genes in Visium data from the snRNA-seq data: *MT-ATP6, MT-ATP8, MT-CO1, MT-CO2, MT-CO3, MT-CYB, MT-ND1, MT-ND2, MT-ND3, MT-ND4, MT-ND4L, MT-ND5, MT-ND6*.

Immunohistochemistry oh post-mortem brain samples

4µm formalin-fixed paraffin-embedded tissue sections were first deparaffinized in 100% RotiHistol twice for 5 minutes and rehydrated by incubating in decreasing concentrations of ethanol (100% twice, 96%, 80%, 70%) for 1 minute each. Sections were then briefly washed with water and boiled for 10 minutes in pre-heated antigen unmasking solution buffer (Vector Laboratories, H-3300, 1:100). After a brief wash, autofluorescence was quenched with an autofluorescence eliminator reagent (EMD Millipore, 2160) for 1 minute followed by a 10-minute incubation with freshly made 3% H2O2, a wash in Tris-buffered saline + 0.5% Triton (TBS-T) and a 1-hour incubation in blocking solution (TBS-T, 10% heat-inactivated horse serum). Sections were incubated in primary antibody diluted in blocking solution at 4°C overnight in a humid chamber. Primary antibodies used for immunohistochemistry were: anti-OLIG2 (rabbit, Sigma-Aldrich, HPA003254, 1:100), anti-Olig2 (goat, R&D Systems, AF2418, 1:200), anti-CNP (mouse, Sigma-Aldrich, AMAB91072, 1:1000), anti-MT-ND4 (rabbit, Invitrogen, PA5-116791, 1:200), anti-AACT (SERPINA3) (rabbit, Abcam, AB205198, 1:1000), anti-CD31 (goat, R&D Systems, AF3628-SP, 1:100). The next day the sections were washed in TBS-T and incubated for 2 hours with the matching secondary peroxidase-conjugated antibody. Secondary antibodies that were used: ImmPRESS IgG Polymer Kits, Peroxidase, Vector Laboratories (horse anti-goat, MP-7405; horse anti-rabbit, MP-7401; horse anti-mouse, MP-7402). After washing the

315 sections in TBS-T, they were incubated with fluorophore diluted 1:500 in borate buffer solution (100 mM
316 borate buffer, 0.003% H2O2) for 10 minutes. The fluorophores used were TSA Vivid Fluorophore 520, 570
317 and 650 (Bio-Techne, 7523/1, 7526/1, 7527/1). Multiplexed stainings were done sequentially, performing the
318 incubation of each primary antibody separately overnight, after repeating the antigen retrieval step with the
319 boiling time reduced to 3 minutes. Nuclei were counterstained with DAPI diluted 1:1000 in PBS for 3 minutes
320 and slides were washed in PBS and mounted with Fluoromount-G (0100-01, Southern Biotech).

321 Images of the entire human brain sections were acquired with the Pannoramic Midi II Slide Scanner (3D
322 HISTEC) with the 20x objective. Scans were converted into tiff-files using the NGFF-Converter (Glencoe
323 Software) and for each patient, approximately 10 random images of similar size were selected per each
324 cortical layer set and cells were quantified manually or semi-quantitatively with the cell-counter plugin.

325 **Statistics**

326 No statistical methods were used to predetermine sample sizes, but our sample size for the snRNA-seq and
327 the validation experiments was comparable to previously published studies. For the snRNA-seq analyses
328 Python- and R-based open source packages were used and the statistical analysis is described in the
329 dedicated methods section. For the immunohistochemical validations, graphical visualizations and statistical
330 analysis were performed using GraphPad Prism software (10.3.1). Differences between two groups were
331 determined using a student's t-test. For statistically significant comparisons ($p<0.05$) exact p-values are
332 displayed in the figures, all other comparisons did not show a significant p-value.

333 **Data availability**

334 We obtained preprocessed reads from one publicly available dataset that performed single-nucleus RNA-seq
335 in AD patients (Gabitto et. al, 2024)[16]. This dataset can be accessed through AWS (https://sea-ad-single-cell-
336 profiling.s3.amazonaws.com/index.html#MTG/RNAseq/Supplementary%20Information/Nebula%20Results
337 /.)

338 Our own generated (snRNA-seq and Visium) data will be made available upon acceptance of the manuscript.

339 **Code availability**

340 The collection of scripts used to annotate the snRNA-seq & Visium data and publicly available datasets,
341 perform all the analyses and create each figure are available at the Jaekel lab github page:
342 https://github.com/Jaekellab/human_AD_snRNAseq/tree/main.

343 **Acknowledgments**

344 We want to thank the following people for their contribution to the manuscript: Felix Fischer for setting up
345 the analysis and the notebook structure for the bioinformatic analysis. Vladimir Shitov and Daniel Strobl for
346 the guidance on the cellranger output. Michaela Müller for the help with integration and access to the
347 scAtlasTab pipeline. Will Macnair and Sergio Marco-Salas for the helpful feedback on the figures and the
348 manuscript. All the developers of the tools that have been used and the sc-best-practices consortium for the
349 tutorials and environment files. Finally, we thank all the member from the group of FT and SJ for their
350 insightful discussions, feedback, and support.

351 **Author contributions**

352 S.J. designed the study and together with F.J.T. supervised the project. C.H. performed snRNA and visium
353 experiments and performed the library preparations with the help of E.B. F.D. wrote the code and performed

354 bioinformatic data analysis under the supervision of F.J.T. and L.K. S.J. and F.D. interpreted the results from
355 the data analysis; N.D. and S.J. performed experimental validations. F.D designed and created the figures and
356 together with S.J. wrote the manuscript. All authors read, corrected and approved the manuscript.

357 **Competing interests**

358 F.J.T. consults for Immunai, CytoReason, BioTuring, Genbio and Valinor Industries, and has ownership interest
359 in RN.AI Therapeutics, Dermagnostix, and Cellarity. S.J. has a financially supported research collaboration
360 with Ono Pharmaceuticals.

361 **Funding**

362 S.J. and her research were funded by the DFG Emmy-Noether Programme (JA 2891/2-1) and the Hertie
363 Network of Excellence in Clinical Neuroscience. F.J.T received the following funding: DeepCell: Funded by the
364 European Union (ERC, DeepCell - 101054957), HCA Data Ecosystems: This work was supported by the Chan
365 Zuckerberg Initiative Foundation (CZIF; grant CZIF2022-007488 (Human Cell Atlas Data Ecosystem)), MCML:
366 This work was supported by the German Federal Ministry of Research, Technology and Space (BMFTR) under
367 grant no. 01IS18053A. Leibnizpreis: This work was supported by the DFG Leibniz Prize awarded to F.J.T.

368 **References**

369 1. Kedia, S. & Simons, M. Oligodendrocytes in Alzheimer's disease pathophysiology. *Nat. Neurosci.* **28**, 446–
370 456 (2025).
371 2. Braak, H. & Braak, E. Neuropathological stageing of Alzheimer-related changes. *Acta Neuropathol. (Berl.)*
372 **82**, 239–259 (1991).
373 3. Macnair, W. *et al.* snRNA-seq stratifies multiple sclerosis patients into distinct white matter glial
374 responses. *Neuron* **113**, 396-410.e9 (2025).
375 4. Siletti, K. *et al.* Transcriptomic diversity of cell types across the adult human brain. *Science* **382**,
376 eadd7046 (2023).
377 5. Bhaduri, A. *et al.* An atlas of cortical arealization identifies dynamic molecular signatures. *Nature* **598**,
378 200–204 (2021).
379 6. Mathys, H. *et al.* Single-cell transcriptomic analysis of Alzheimer's disease. *Nature* **570**, 332–337 (2019).
380 7. Mathys, H. *et al.* Single-cell atlas reveals correlates of high cognitive function, dementia, and resilience
381 to Alzheimer's disease pathology. *Cell* **186**, 4365-4385.e27 (2023).
382 8. Liu, A., Fernandes, B. S., Citu, C. & Zhao, Z. Unraveling the intercellular communication disruption and
383 key pathways in Alzheimer's disease: an integrative study of single-nucleus transcriptomes and genetic
384 association. *Alzheimers Res. Ther.* **16**, 3 (2024).

385 9. Behrendt, G. *et al.* Dynamic changes in myelin aberrations and oligodendrocyte generation in chronic
386 amyloidosis in mice and men. *Glia* **61**, 273–286 (2013).
387 10. Tse, K.-H., Cheng, A., Ma, F. & Herrup, K. DNA damage-associated oligodendrocyte degeneration
388 precedes amyloid pathology and contributes to Alzheimer's disease and dementia. *Alzheimers Dement.*
389 **14**, 664–679 (2018).
390 11. Xu, Y. K. T. *et al.* Brain-wide mapping of oligodendrocyte organization and oligodendrogenesis
391 across the murine lifespan. 2024.09.06.611254 Preprint at https://doi.org/10.1101/2024.09.06.611254
392 (2024).
393 12. Heumos, L. *et al.* Best practices for single-cell analysis across modalities. *Nat. Rev. Genet.* **24**, 550–
394 572 (2023).
395 13. Yates, J., Kraft, A. & Boeva, V. Filtering cells with high mitochondrial content depletes viable
396 metabolically altered malignant cell populations in cancer single-cell studies. *Genome Biol.* **26**, 91 (2025).
397 14. Subramanian, A., Alperovich, M., Yang, Y. & Li, B. Biology-inspired data-driven quality control for
398 scientific discovery in single-cell transcriptomics. *Genome Biol.* **23**, 267 (2022).
399 15. Montserrat-Ayuso, T. & Esteve-Codina, A. High content of nuclei-free low-quality cells in reference
400 single-cell atlases: a call for more stringent quality control using nuclear fraction. *BMC Genomics* **25**,
401 1124 (2024).
402 16. Gabitto, M. I. *et al.* Integrated multimodal cell atlas of Alzheimer's disease. *Nat. Neurosci.* **27**, 2366–
403 2383 (2024).
404 17. Desai, R. *et al.* Mitochondria form contact sites with the nucleus to couple prosurvival retrograde
405 response. *Sci. Adv.* **6**, eabc9955 (2020).
406 18. Xin, W. & Chan, J. R. Myelin plasticity: sculpting circuits in learning and memory. *Nat. Rev. Neurosci.*
407 **21**, 682–694 (2020).
408 19. Denholtz, L. E., Liu, J., Nahmoud, I., Casaccia, P. & Likhtik, E. PV - Oligodendrocyte Interactions in
409 the Infralimbic Cortex Promote Extracellular Plasticity after Safety Learning. 2025.07.25.666881 Preprint
410 at https://doi.org/10.1101/2025.07.25.666881 (2025).
411 20. Korotkevich, G. *et al.* Fast gene set enrichment analysis. 060012 Preprint at

412 https://doi.org/10.1101/060012 (2021).

413 21. Sadick, J. S. *et al.* Astrocytes and oligodendrocytes undergo subtype-specific transcriptional changes
414 in Alzheimer's disease. *Neuron* **110**, 1788-1805.e10 (2022).

415 22. Green, G. S. *et al.* Cellular communities reveal trajectories of brain ageing and Alzheimer's disease.
416 *Nature* 1–12 (2024) doi:10.1038/s41586-024-07871-6.

417 23. Cain, A. *et al.* Multicellular communities are perturbed in the aging human brain and Alzheimer's
418 disease. *Nat. Neurosci.* **26**, 1267–1280 (2023).

419 24. Alkallas, R., Fish, L., Goodarzi, H. & Najafabadi, H. S. Inference of RNA decay rate from
420 transcriptional profiling highlights the regulatory programs of Alzheimer's disease. *Nat. Commun.* **8**, 909
421 (2017).

422 25. Kim, K. M. *et al.* Mitochondrial RNA in Alzheimer's Disease Circulating Extracellular Vesicles. *Front.*
423 *Cell Dev. Biol.* **8**, 581882 (2020).

424 26. Falcão, A. M. *et al.* Disease-specific oligodendrocyte lineage cells arise in multiple sclerosis. *Nat.*
425 *Med.* **24**, 1837–1844 (2018).

426 27. Zhou, Y. *et al.* Human and mouse single-nucleus transcriptomics reveal TREM2-dependent and
427 TREM2-independent cellular responses in Alzheimer's disease. *Nat. Med.* **26**, 131–142 (2020).

428 28. Kenigsbuch, M. *et al.* A shared disease-associated oligodendrocyte signature among multiple CNS
429 pathologies. *Nat. Neurosci.* **25**, 876–886 (2022).

430 29. Pandey, S. *et al.* Disease-associated oligodendrocyte responses across neurodegenerative diseases.
431 *Cell Rep.* **40**, (2022).

432 30. Wang, X., He, Y., Zhang, Q., Ren, X. & Zhang, Z. Direct Comparative Analyses of 10X Genomics
433 Chromium and Smart-seq2. *Genomics Proteomics Bioinformatics* **19**, 253–266 (2021).

434 31. Wolf, F. A., Angerer, P. & Theis, F. J. SCANPY: large-scale single-cell gene expression data analysis.
435 *Genome Biol.* **19**, 15 (2018).

436 32. Clarke, Z. A. & Bader, G. MALAT1 expression indicates cell quality in single-cell RNA sequencing
437 data. 2024.07.14.603469 Preprint at https://doi.org/10.1101/2024.07.14.603469 (2024).

438 33. Young, M. D. & Behjati, S. SoupX removes ambient RNA contamination from droplet-based single-

439 cell RNA sequencing data. *GigaScience* **9**, giaa151 (2020).

440 34. Wolock, S. L., Lopez, R. & Klein, A. M. Scrublet: Computational Identification of Cell Doublets in
441 Single-Cell Transcriptomic Data. *Cell Syst.* **8**, 281-291.e9 (2019).

442 35. Ahlmann-Eltze, C. & Huber, W. Comparison of transformations for single-cell RNA-seq data. *Nat.*
443 *Methods* **20**, 665–672 (2023).

444 36. Sikkema, L. *et al.* An integrated cell atlas of the lung in health and disease. *Nat. Med.* **29**, 1563–1577
445 (2023).

446 37. Lopez, R., Regier, J., Cole, M. B., Jordan, M. I. & Yosef, N. Deep generative modeling for single-cell
447 transcriptomics. *Nat. Methods* **15**, 1053–1058 (2018).

448 38. Xu, C. *et al.* Probabilistic harmonization and annotation of single-cell transcriptomics data with
449 deep generative models. *Mol. Syst. Biol.* **17**, e9620 (2021).

450 39. Luecken, M. D. *et al.* Benchmarking atlas-level data integration in single-cell genomics. *Nat.*
451 *Methods* **19**, 41–50 (2022).

452 40. Luecken, M. D. *et al.* Defining and benchmarking open problems in single-cell analysis. *Nat.*
453 *Biotechnol.* 1–6 (2025) doi:10.1038/s41587-025-02694-w.

454 41. Zappia, L. & Oshlack, A. Clustering trees: a visualization for evaluating clusterings at multiple
455 resolutions. *GigaScience* **7**, giy083 (2018).

456 42. Mathys, H. *et al.* Single-cell multiregion dissection of Alzheimer's disease. *Nature* 1–11 (2024)
457 doi:10.1038/s41586-024-07606-7.

458 43. Love, M. I., Huber, W. & Anders, S. Moderated estimation of fold change and dispersion for RNA-
459 seq data with DESeq2. *Genome Biol.* **15**, 550 (2014).

460 44. Liberzon, A. *et al.* Molecular signatures database (MSigDB) 3.0. *Bioinformatics* **27**, 1739–1740
461 (2011).

462 45. Büttner, M., Ostner, J., Müller, C. L., Theis, F. J. & Schubert, B. scCODA is a Bayesian model for
463 compositional single-cell data analysis. *Nat. Commun.* **12**, 6876 (2021).

464 46. Heumos, L. *et al.* Pertpy: an end-to-end framework for perturbation analysis. 2024.08.04.606516
465 Preprint at https://doi.org/10.1101/2024.08.04.606516 (2024).

466 47. NEBULA is a fast negative binomial mixed model for differential or co-expression analysis of large-
467 scale multi-subject single-cell data | Communications Biology. https://www.nature.com/articles/s42003-
468 021-02146-6#article-info.
469 48. Totty, M., Hicks, S. C. & Guo, B. SpotSweeper: spatially aware quality control for spatial
470 transcriptomics. *Nat. Methods* **22**, 1520–1530 (2025).
471

472 **Figure legends**

473 **Figure 1: Cell type specific transcriptional profiles diverge across brain areas in AD pathology.**

474 **A** Study design showing snRNA-seq analysis of 13 donors across 3 brain regions (prefrontal, temporal and
475 visual cortex) with nuclei isolation and sequential computational analysis of oligodendrocytes. **B-D** UMAP
476 visualizations of all cell types after QC (n = 26,598 nuclei), with major cell populations (**B**), conditions - AD vs
477 Control - (**C**) and cortical areas (**D**). **E** Percentage distribution of cellular composition across conditions and
478 cortical areas (PFC, TC, VC). **F** Dotplot of selected marker genes for broad cell type annotation. **G**
479 Representative immunofluorescence images of AD patient brains and quantifications of CNP+ OLIG2-/SOX10-
480 oligodendrocytes in human brain tissue (n = 4 individuals per group), demonstrating a decrease of canonical
481 marker expression in oligodendrocytes in AD. Scale bar = 50µm. **H** Quantifications of CNP+ oligodendrocytes
482 (green arrows) across cortical layers in the visual and temporal cortices in control and AD brains (n = 7-8
483 individuals per group). Scale bar= 20µm. **I** Mean expression of canonical marker genes for astrocytes,
484 microglia and oligodendrocytes between control and AD, demonstrating a general loss in AD.

485 **Figure 2: Mitochondrial gene expression varies across cortical areas and in disease.**

486 Pre-quality control analysis showing percentage of mitochondrial (*MT*) and nuclear fractions for all cells
487 across **A** different Braak stages and **B** different cortical regions. **C** The percentage of low (<15%) and high
488 (>15%) *MT* fraction shown per cell type and condition. **D** Visium analysis of temporal and visual cortices from
489 control and AD brain samples. Upper panels show H&E staining with cortical layers and gray matter (GM)
490 boundaries marked. Lower panels display spatial distribution of *MT* gene fractions across tissue sections.

491 **Figure 3: Oligodendrocyte subtypes vary across cortical areas and in disease.**

492 **A** UMAP plot of oligodendrocyte suptypes (n= 9030). **B** Bar plots depicting the fraction of cells per condition
493 and area distributed across OL subtypes. **C** UMAP plots of OL with gaussian kernel density estimates over
494 area and condition. **D** Bar plot depicting the percentage of up- and down-regulated differentially expressed
495 genes (adjusted p-value < 0.05) across oligodendrocyte subtypes identified with DESeq2. **E** Dotplot showing
496 oligodendrocyte subset markers based on DE analysis. **F** Heatmap showing the confusion matrix comparing
497 OL annotations with a recently published reference dataset[16]. **G** Functional characterization of OL subclusters
498 via pathway analysis, indicating normalized expression scores (p-value < 0.05) from each pathway; selected
499 relevant genes of each pathway are displayed on the left. **H** Representative images and quantifications of
500 MT-ND4+ OLIG2+ oligodendrocytes in the temporal and visual cortices of post-mortem human brains (n = 6
501 individuals per group). Scale bar = 25µm.

502 **Extended Data Figure 1: General quality control metavariables to determine outliers.**

503 **A-C** Violin plots showing the number of identified counts and genes (**A**), mitochondrial fractions (**B**) and
504 *MALAT1* expression (**C**) across all samples. Abbreviations: AS - area striata (part of the visual cortex), GR -
505 Gyrus Rectus (part of the prefrontal cortex, TG - Temporal Gyrus (part of the temporal cortex). Samples
506 highlighted by a red rectangle were removed for further analysis. **D** UMAP plots of leiden clusters (res=1.0),
507 log1p_counts, *MALAT1*-expression and *MT*-fraction over the entire dataset for quality control.

508 **Extended Data Figure 2: Mixed lineage cluster cells express oligodendrocyte, astrocyte and neuronal**
509 **marker genes.**

510 **A** Unannotated cells (n=2670) highlighted in the UMAP plot of the complete, quality controlled data. **B**
511 Dotplot of canonical marker genes in these unannotated cells demonstrating the expression of mixed-lineage
512 markers**,** emphasizing astrocyte (*SLC1A2*), oligodendrocyte (*MBP*, *PLP1*) and Inhibitory neurons (*SYT1*)
513 markers. Additionally, previously reported mixed-lineage markers[3] (*RBFOX1*, *PDE4B*) are expressed. **C** The
514 integrated mixed-lineage cluster UMAPs colored by condition and cortical area show higher separation
515 between conditions than areas. **D** UMAP overlay of MT and nuclear fractions in unannotated cells. **E** Examples
516 of immunohistochemical stainings of individual cells in AD brains showing co-labelling of the EC marker CD31
517 and the mature OL marker CNP (orange arrows). CNP+ OL that are CD31- are indicated by green arrows. Scale
518 bars: 10µm.

519 **Extended Data Figure 3: Canonical marker gene expression is changed in individual cell types in lzheimer's**
520 **disease.**

521 **A** Quantifications of OLIG2 and CNP+ cells in the TC and VC in Control and AD tissue. **B** Representative images
522 and quantifications of CD31+ EC in the temporal cortex in control and AD. Scale bar = 50µm. **C** Comparison
523 of the sample-wise mean expression of canonical marker genes for each cell type between control and AD.

524 **Extended Data Figure 4: *MT* - and nuclear fractions vary across different conditions.**

525 **A** Percentage of *MT* fraction and *MALAT1* expression for all cells across condition and cortical area in this
526 dataset. **B** Quality control filtering matrix shows the number of cells removed by different thresholds, based
527 on number of genes detected, UMI counts, mitochondrial fraction, and *MALAT1* expression, across conditions
528 and cortical areas. **C** Percentage of *MT* and nuclear fractions for all cells across Braak stages and regions from
529 Gabitto et al., 2024.

530 **Extended Data Figure 5: Quality control results are more confounded with regional differences in AD slides**
531 **than control slides.**

532 Quality control analysis with SpotSweeper[48] providing results for global and local outliers. Global outliers in
533 slides from a control (**A**) and AD patient (**B**) seem to follow coherent patterns rather than random allocations
534 suggesting that high thresholds pick up on regional differences. For each control and AD subject two slides
535 from temporal and visual cortices are shown with log2 total and detected counts. From the results we can
536 show that no slide shows artifacts of 1) dryspots - not visible in histological images, identified by low library
537 sizes and no difference in mitochondrial ratio or 2) hangnail artefacts - library sizes and no difference in
538 mitochondrial ratio.

539 **Extended Data Figure 6: Regional density distributions per cell type mirror Alzheimer's disease progression**
540 **gradient.**

541 UMAPs showing the kernel dentistry estimation (scanpy.tl.embedding_density) in all broad cell types
542 (besides OL) across the temporal, prefrontal, and visual cortex. Regional gradients reflect decreasing AD

543 pathology from lowest (visual cortex) to highest pathology (temporal cortex), based on pathological
544 assumptions thereby providing a spatial snapshot of cellular changes along disease progression.

545 **Extended Data Figure 7: Common disease-associated oligodendrocyte markers are not expressed.**

546 **A** Dotplot showing the log-scales mean expression of common disease-associated OL (DAO) genes taken from
547 the literature and divided into four groups: 1) transcription factors (TFs), 2) reactive markers, 3) immune-
548 response genes and 4) genes associated with cholesterol metabolism. While TF expression might be lower in
549 snRNA-seq vs scRNA-seq, other frequently cited DAO genes, such as *SERPINA3*, also do not show high
550 expression. **B** Representative images and quantifications of immunohistochemical stainings of
551 SERPINA3+OLIG2+ OL in human brains across cortical layers in the temporal cortex demonstrating a low
552 abundance of SERPINA3+ OL and no specific enrichment in AD. Scale bars: 50 µm. **C-E** Analysis of *SERPINA3*
553 expression in the temporal cortex; snRNA-seq data from Gabitto et al., 2025. UMAP of all cell types (OL solid
554 circle, astrocytes dashed circle) (**C**). UMAP overlay of *SERPINA3* expression across celltypes, with the highest
555 enrichment observed in astrocytes rather than oligodendrocytes (**D**). Dotplot showing commonly reported
556 DAO genes in OL, supporting the observation that *SERPINA3* is not highly expressed in disease OL (**E**). **F-H**
557 Parallel analysis of SERPINA3 expression in dorsolateral prefrontal cortex (DLPFC); snRNA-seq data from
558 Gabitto et al., 2025. UMAP of all cell types (OL solid circle, astrocytes dashed circle) (**F**). UMAP overlay of
559 *SERPINA3* expression across cell types, with the highest enrichment observed in astrocytes rather than
560 oligodendrocytes, consistent with temporal cortex findings (**G**). Dotplot showing oligodendrocyte-specific
561 marker gene expression in DLPFC, confirming the absence of SERPINA3 expression in oligodendrocytes across
562 different cortical regions (**H**).